Naturaliste Plateau: Constraints on the timing and evolution of the Kerguelen Large Igneous Province and its role in Gondwana breakup

N. G. Direen[a, b]*, B. E. Cohen[c, d], R. Maas[e], F. A. Frey[f], J. M. Whittaker[b], M. F. Coffin[b, g], S. Meffre[a, h], J. A. Halpin[a, b, h] and A. J. Crawford[a, h].

[a] School of Physical Sciences, University of Tasmania, Private Bag 126, Hobart TAS 7001, Australia

[b] Institute for Marine and Antarctic Studies, University of Tasmania, Private Bag 129, Hobart TAS 7001, Australia

[c] School of Earth Sciences, The University of Queensland, St Lucia QLD 4072, Australia

[d] Scottish Universities Environmental Research Centre, East Kilbride, G75 0QF, UK

[e] School of Earth Sciences, University of Melbourne, Parkville, VIC 3010, Australia

[f] Earth, Atmosphere and Planetary Sciences, Massachusetts Institute of Technology, Cambridge, MA 02139-4307, USA

[g] Woods Hole Oceanographic Institution, Woods Hole, MA 02543-1050, USA

[h] ARC Centre of Excellence in Ore Deposits and School of Physical Sciences, University of Tasmania, Private Bag 126, Hobart TAS 7001, Australia

*Corresponding author: email n_direen@utas.edu.au; cell +1 727-517-6874

Postal address: 2523 Bridgestone Park Ln, Spring TX 77386 USA

SUPPLEMENTARY PAPERS

Australian Journal of Earth Sciences (2017) *64 (7),*

http://dx.doi.org/10.1080/08120099. 2017.1367326

Supplementary papers

Appendix 1. Photographs of dredge samples, RV Southern Explorer voyage 2005.
Appendix 2. Major and trace element analysis (University of Tasmania).
Appendix 3. Laser-ablation ICP-MS U–Pb zircon dating (University of Tasmania).
Appendix 4. $^{40}Ar/^{39}Ar$ dating of plagioclase (University of Queensland).
Appendix 5. Radiogenic (Sr–Nd–Hf–Pb) isotopes (University of Melbourne).

Appendix 1. Photographs of dredge samples, RV Southern Explorer voyage 2005/09. Scale is an Australian 20 cent piece.

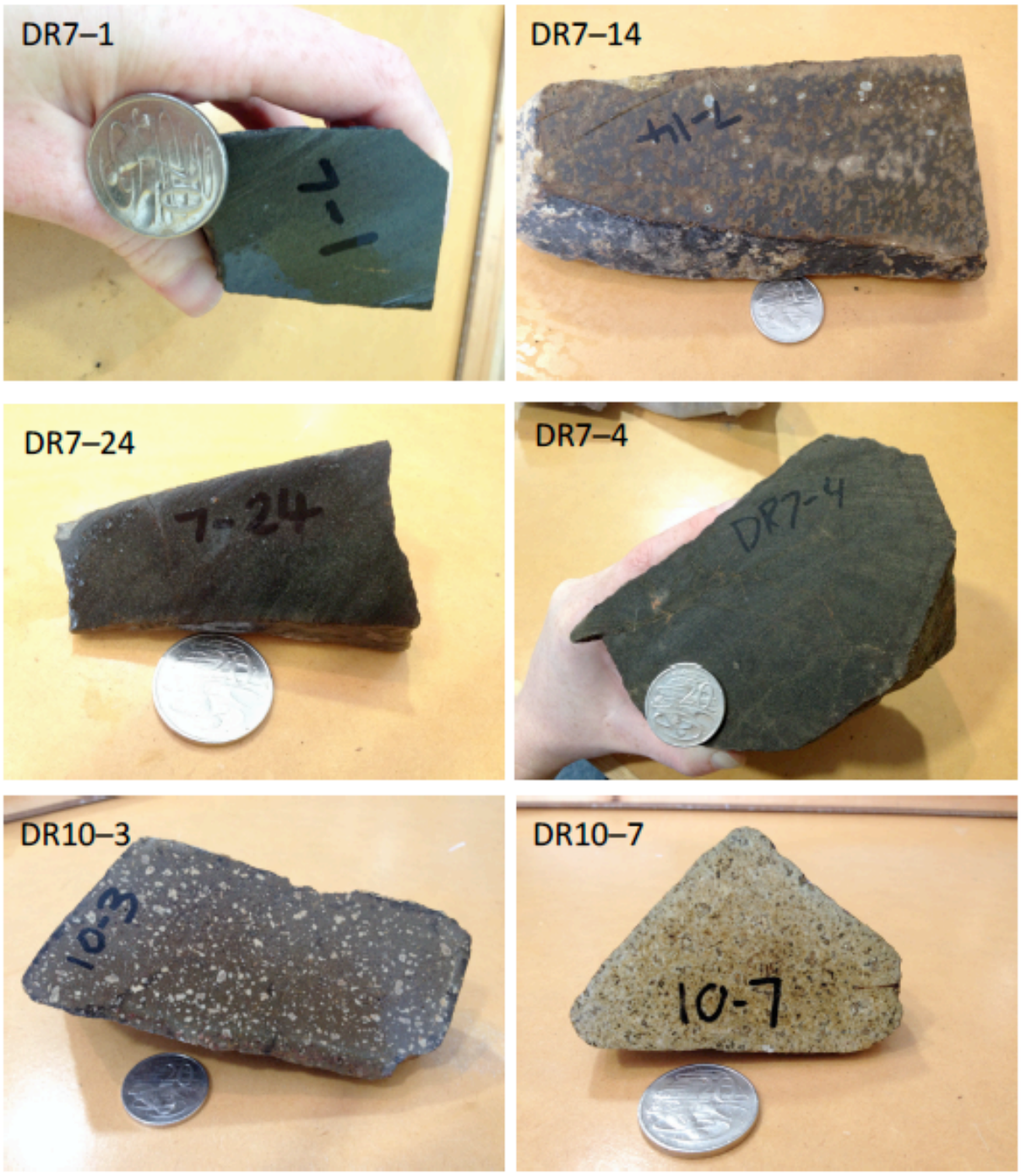

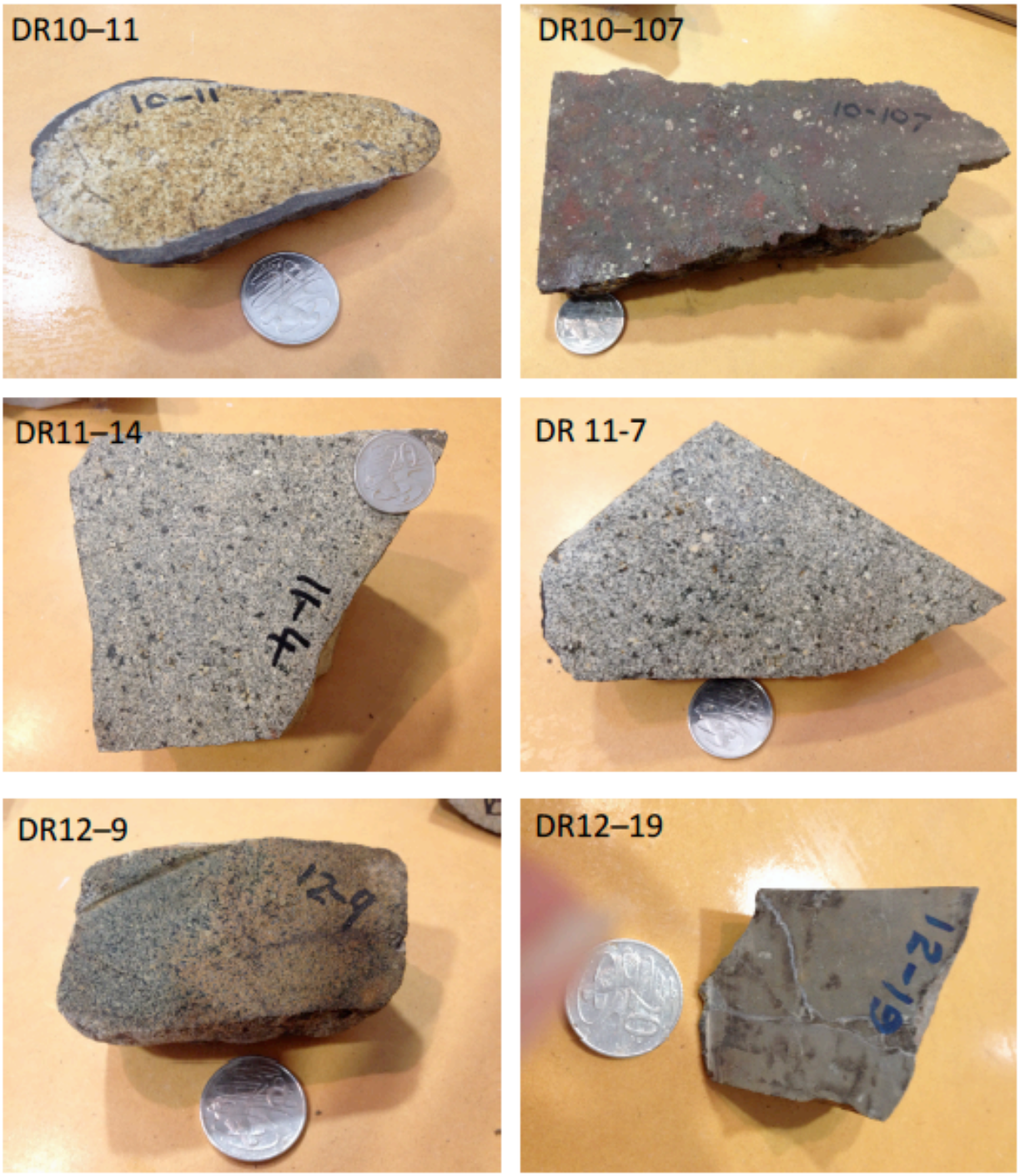
DR10–11
DR10–107
DR11–14
DR 11-7
DR12–9
DR12–19

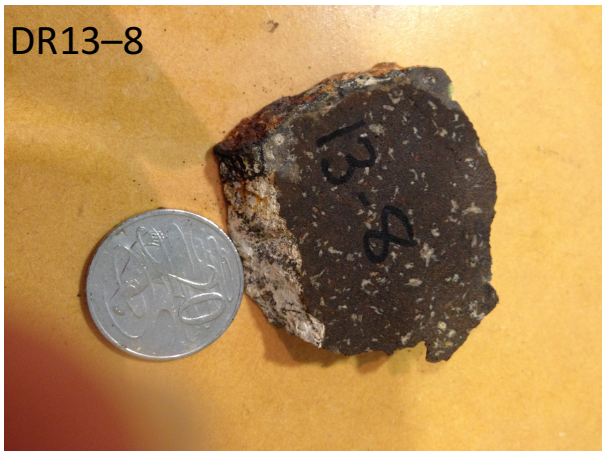
DR13–8
13-8


DR13–17
13-17


DR13–22
13-22


DR13–58
13-58

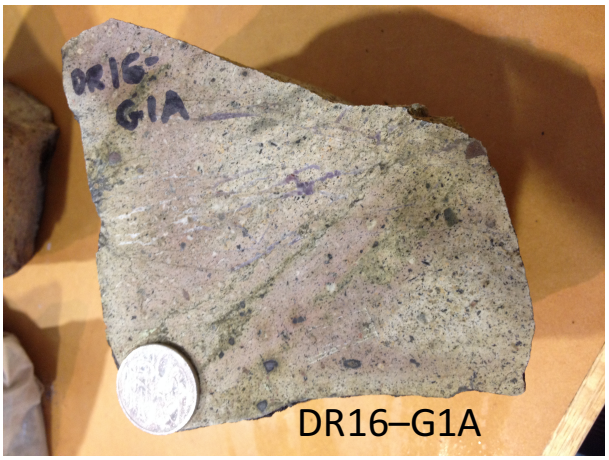
DR16-G1A
DR16–G1A

Appendix 2. Major and trace element analysis (University of Tasmania)

Sample powders for bulk rock major and trace element analysis were prepared in a tungsten carbide mill. Concentrations of major elements and 13 trace elements (Rb, Sr, Ba, Sc, Cr, V, Ni, Cu, Zn, Zr, Nb, Y, Ce) were determined by X-ray fluorescence (XRF), using fused discs prepared with 12 $Li_2B_4O_7$–22 $LiBO_2$ and a sample-flux ratio of 1:9 in non-wetting 5% Au–95% Pt crucibles at 1100˚C, and pressed powder (10 g) buttons, respectively (e.g., Falloon et al., 2007). The discs and buttons were analysed using a Phillips PW1480 X-ray spectrometer equipped with LiF200, LiF220, PX-1, PE002 and Ge111 crystals. Corrections for mass absorption were calculated using Phillips X40 software with De Jongh's calibration model and Phillips alpha coefficients. Calibration was achieved using pure element mixes in pure silica, along with international and in-house rock standards. Major and trace element results for international standard rocks are reported in Falloon et al. (2007). Concentrations of 34 trace elements (incl. rare earth elements) were determined by solution-mode inductively-coupled plasma mass spectrometry (ICP-MS, Robinson et al., 1999; Yu et al., 2000). Analyses were done on duplicate digestions after high-pressure dissolutions with HF–$HClO_4$ (Yu et al., 2001). Elemental abundances measured by both XRF and ICP-MS generally show good agreement, with correlation coefficients close to 1.

Appendix 3. Laser-ablation ICP-MS U–Pb zircon dating (University of Tasmania)

Zircons from granophyre DR10-16, monzodiorite DR11-6 and a rhyolite DR12-29 were separated from 200 g of rock crushed in a Cr-steel ring mill for 10 seconds; this produced medium to coarse sand. Non-magnetic heavy minerals were separated from the crushed material using a gold pan and a Fe–B–Nd hand magnet. Zircons were hand-picked from the non-magnetic heavy mineral concentrate under the microscope in cross-polarised transmitted light. The selected crystals were placed on double-sided sticky tape and fixed in epoxy resin within 2.5 cm diameter moulds. After curing for 12 hours, the mounts were polished using sandpaper and a polishing lap and ultrasonicated in distilled water prior to analysis.

Laser sampling U–Th–Pb isotope analyses were performed with a 213 nm New Wave Research solid state laser interfaced with an Agilent 7500cs quadrupole ICP-MS. Ablations were done within a custom-made, low-volume ablation cell in a helium athmosphere. Pb/U down-hole fractionation, instrument drift and mass bias corrections were constrained using 417 Ma Temora zircon (Black et al., 2003) as the primary standard. Temora zircon was analysed twice at the start and end of each session, and after every 12 unknowns, or approx.. every 30 minutes. This spacing was found to provide the best drift correction for the analytical set-up used. Analysis of fewer standards analysed more frequently can lead to problems with over-fitting of the drift correction curves and increases age scatter in unknowns. Three zircons (91500, Mud Tank, 98-521, Black et al., 2003; Black and Gulson, 1978; Harris et al., 2004) were analysed as secondary standard between each batch of samples. Standards an unknowns were analysed using the same ablation conditions (spot size, repetition rate). Mass bias and drift for the $^{207}Pb/^{206}Pb$ ratio was corrected using large spots on NIST610 analysed after every 36 unknown zircons.

Ablations of zircons (32 μm laser spot, 5 Hz, power density 12 Jcm^{-2}) began with a 30 second gas blank, followed by 30 seconds with the laser switched on. Ablation products were swept from the chamber using a He gas flow and carried to the ICP-MS torch in a flow of high-purity argon gas. Dwell times for ^{96}Zr, ^{146}Nd, ^{178}Hf, ^{202}Hg, ^{232}Th and ^{238}U were 10 ms, those for ^{204}Pb, ^{206}Pb, ^{207}Pb and ^{208}Pb were 30 ms, completing a complete sweep every 190 ms. ^{235}U was calculated from ^{238}U assuming $^{238}U/^{235}U = 137.88$. The data reduction method used was similar to that reported in Sack et al. (2011) and propagation of uncertainties was similar to that described by Paton et al. (2010). Time-resolved signal traces were examined on the concordia diagram to eliminate zones with Pb-rich inclusions or Pb loss from the calculations, similar to the VizualAge technique described in Petrus and Kamber (2012).

Elemental abundances were calculated using Zr (400 000 ppm) as internal standard element, and using the 91500 zircon to correct for mass bias and drift.

The LA-ICP-MS results are listed in Table A3 and shown in Figure A3.2. Data points are plotted with 1 sigma errors to avoid cluttering, but age uncertainties calculated by Isoplot (Ludwig, 2009) are quoted at 2 sigma. Decay constants are from Steiger and Jäger (1977).

Table A3 U–Th–Pb isotope results for zircons in igneous rocks from the southern Naturaliste Plateau (Excel file).

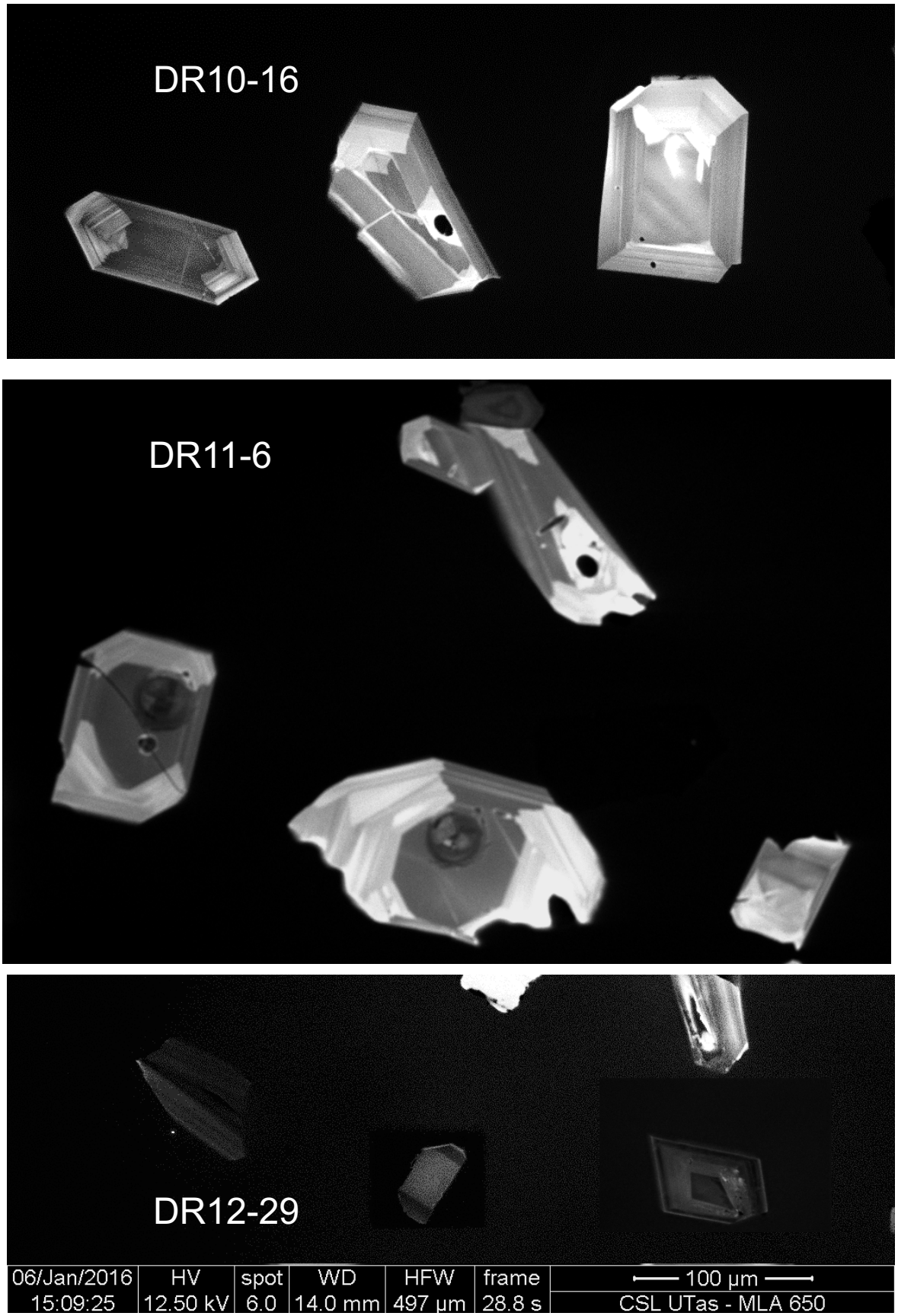

Figure A3.1 Cathodoluminescence images of zircons: granophyre DR10-16, monzodiorite DR11-6 and rhyolite (DR12-29).

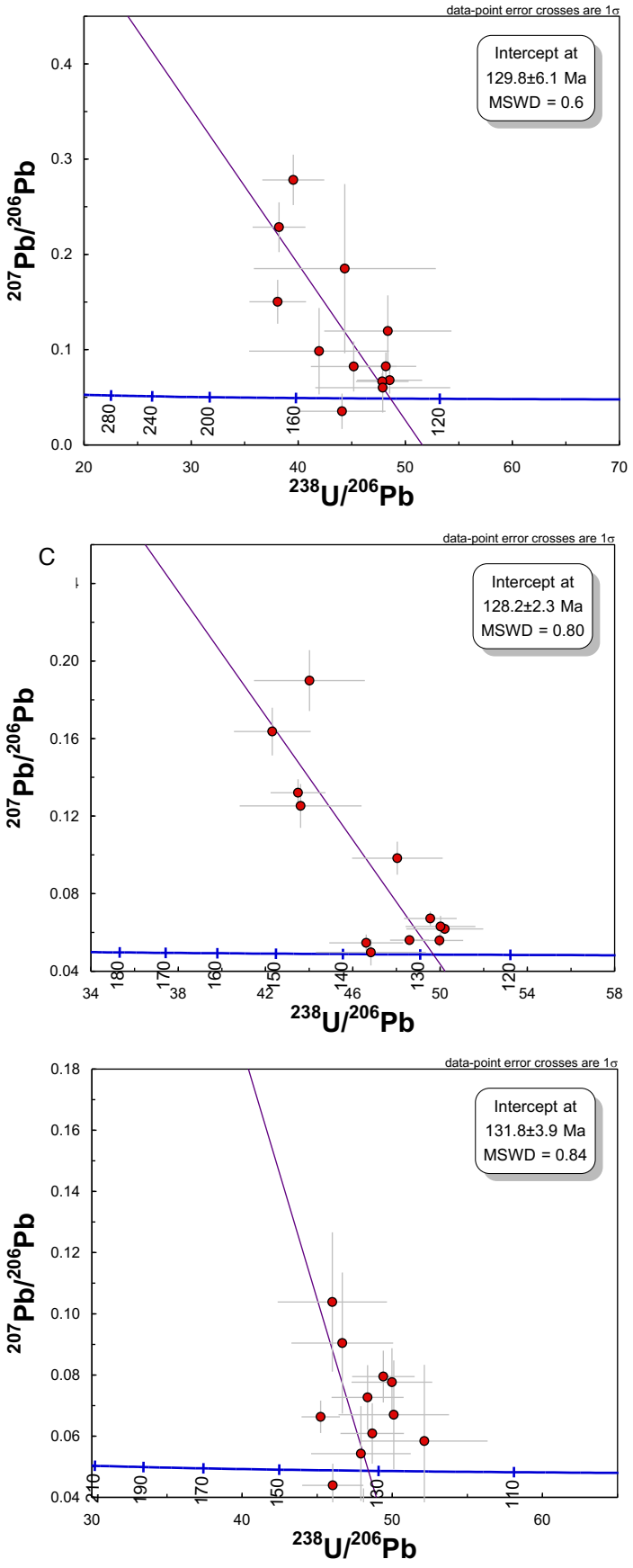

Figure A3.2 Tera-Wasserburg U–Pb concordia diagrams for zircons from rhyolite DR12-29 (top), monzodiorite DR11-6 (middle) and granophyre DR10-16 (bottom). Error bars are 1σ but age errors are 2σ, see main text. Common Pb corrections anchored at 128 Ma on the crustal growth curve of Stacey and Kramers (1975).

Appendix 4. $^{40}Ar/^{39}Ar$ dating of plagioclase (University of Queensland)

Samples for $^{40}Ar/^{39}Ar$ geochronology were selected based on the appearance of plagioclase phenocrysts or microphenocrysts within rocks that were least affected by seafloor alteration. The freshness of plagioclase was examined by thin section petrography. Sample DR11-19 contains plagioclase phenocrysts up to 5 mm long in a grey groundmass; DR12-8 has plagioclase laths <1 mm long set in a mid-brown groundmass; and DR13-33 has plagioclase phenocrysts up to 15 mm long set in a light-brown groundmass.

In preparation for plagioclase separation, the rock samples were crushed and sieved to the dimensions listed in the table below, and ultrasonicated in water to remove dust. Plagioclase was separated by firstly using a Franz Isodynamic Separator to remove the magnetic fraction, followed by heavy-liquid separation using LST fluid, with density controlled by the addition of distilled water. To remove clays and other adhering alteration phases, the resultant separate was cleaned in an ultrasonic bath using sequential washes of tap water, distilled water, and distilled water plus ethanol. Each wash lasted approximately 1 hour. The separates were air-dried, and plagioclase crystals handpicked under a binocular microscope. Optically clear crystals were selected, avoiding areas of iron staining, cloudiness, or inclusions of other minerals, melt, or fluid.

Plagioclase separates were wrapped in Al-foil, and placed in 7-pit Al disks, with grains of Fish Canyon sanidine (28.294 ± 0.072 Ma, 2σ, Renne et al., 2011) and GA1550 biotite (99.738 + 0.208 Ma, 2σ, Renne et al., 2011) loaded into separate pits. The irradiation disks were closed with aluminium covers, wrapped in aluminium foil, and vacuum heat-sealed into quartz vials. These quartz vials were irradiated for 14 hours at the B-1 Cadmium-lined in-core irradiation tube facility at the Radiation Center, Oregon State University, USA. Before analysis, the mineral grains and fluence monitors were baked-out under vacuum at ~200°C for ~12 hours. J-factors were calculated using laser total-fusion analyses of 15 single Fish Canyon sanidine crystals from each disk. Four aliquots of GA1550 biotite were also analysed via the laser heating device, and the results provide an important cross-check on the J factors.

Sample	Lab #	Weight plagioclase analysed (mg)	Weight aluminium foil (mg)	Grain size (μm)	Decay (months)
DR11-19	4565-01	86	30	106–425	10
DR12-8	4570-01	90	30	106–425	10
DR13-33	4558-01	74	34	355–1000	5

After a decay period spanning 5 months (for sample DR13-33) or 10 months (for samples DR11-19 and DR12-8), the samples were incrementally heated in a double-vacuum resistance furnace fitted with an Omega temperature controller. For each heating step, the samples (and Al-foil wrapping) were held at the required temperature for a minimum of six minutes. The gas released in each step was cleaned through a cryo-cooled cold trap (T = –137°C) and two C-50 SAES Zr–V–Fe getters (one hot, the other at room temperature of 20°C). Room-temperature blanks, hot blanks (500°C) and room-temperature air pipettes were analysed before and after each sample. For all analyses (blanks, airs, and unknowns) the first stage clean-up (gas exposed to the hot getter and cold finger) lasted for 2100 seconds (35 minutes), and the second stage clean-up (gas also exposed to the room-temperature getter) lasted for 420 seconds (7 minutes). The gas was then inlet to a MAP-215-50 noble gas mass spectrometer equipped with a third C-50 SAES Zr–V–Fe getter (at room temperature) for Ar isotope analysis. Data were collected in peak-hopping mode, with eight cycles of data collection at masses 40, 39, 38, 37, 36, and multiplier baseline. Raw data were corrected for blanks, mass discrimination, nucleogenic interferences and atmospheric contamination, followed by calculation of apparent ages for each degassing step. Data handling was done using the software "MassSpec Version 8.131" developed by Alan Deino of the Berkeley Geochronology Centre, USA. Mass discrimination corrections were based on an average discrimination factor of 1.00217 ± 0.00408 (2σ, n = 40) and the power law, and the $^{40}Ar/^{36}Ar$ value of atmospheric argon is 298.56 ± 0.31 (Lee et al., 2006, Renne et

al., 2009). Further details can be found in Deino and Potts (1990) and Vasconcelos et al. (2002). All ages are reported using the potassium decay constants of Steiger and Jäger (1977). All decay constants and irradiation parameters used are reported in Table A4.1

Plagioclase $^{40}Ar/^{39}Ar$ results

In this study we define an age plateau as a sequence of three or more contiguous steps, corresponding to at least 50% of the total ^{39}Ar released, with apparent ages that overlap within 2σ uncertainties (Fleck et al., 1977; McDougall & Harrison, 1999). Plateau ages were calculated as the mean weighted by inverse variance. Plateau age uncertainties were calculated as the standard error of the weighted mean, but if the MSWD was greater than 1, then the uncertainties were calculated as the standard error of the weighted mean multiplied by the square root of the MSWD. The plateau age uncertainties are 2σ and include the uncertainty in J, but do not include the uncertainty in the potassium decay constants.

Isochrons are plotted for plateau steps only; magenta-coloured ellipses represent the non-plateau steps that were eliminated from the isochron age calculation (Fig.4). The light-brown dashed lines on isochrons indicate the 2σ uncertainty envelopes. Isochron ages were calculated from the $^{39}Ar/^{40}Ar$ intercept, and isochron age uncertainties were calculated using a York regression (York 1969). Isochron age uncertainties are reported at the 95% confidence level (2σ), and include the uncertainty in the irradiation correction factors and the uncertainty in J, but do not include the uncertainty in the potassium decay constants.

Analyses from DR11-19 and DR12-8 yield precise results, reflecting their relatively high K/Ca and $\%^{40}Ar^*$ values. Analyses from DR13-33 are less precise, reflecting the lower K/Ca and $\%^{40}Ar^*$ yields. For both DR11-19 and DR12-8 the $\%^{40}Ar^*$ values decrease at the higher-temperature end of the heating schedule, reflecting an increased atmospheric argon contribution from heating of the resistance furnace itself.

Plateaus comprise 64 to 82% of the ^{39}Ar released, indicating that these results are reliable determinations for the age of eruption. Low-temperature steps yield younger ages characteristic of some argon loss, likely via incipient seawater alteration of the plagioclase. The reliability of the ages is supported by the concordance between the $^{40}Ar/^{39}Ar$ isochron and $^{40}Ar/^{39}Ar$ plateau ages, the excellent agreement between GA1550 analyses 99.8 ± 0.8 Ma (2σ, n = 31) and the accepted age for this material (99.738 + 0.208 Ma, 2σ, Renne et al., 2011), as well as the concordance between the $^{40}Ar/^{39}Ar$ and zircon U–Pb ages. Initial $^{40}Ar/^{36}Ar$ values on isochron diagrams are within analytical uncertainty of modern-day atmosphere, indicating these samples are free from inherited argon.

Table A4 Ar–Ar isotope results. (Excel file)

Appendix 5. Radiogenic (Sr–Nd–Hf–Pb) isotopes (University of Melbourne)

Whole rock isotopic compositions were determined on same rock powders used for major and trace element analyses (Sr, Nd, Hf) or on handpicked chips (Pb). Prior to dissolution for the isotopic work, powders and chips were leached in hot 6M hydrochloric acid (100^{o}C, 1 hour) and subsequently rinsed with distilled water. Low-pressure dissolutions of the residues were done on a hotplate (3:1 HF–HNO_3, 2 days, 100^{o}C; 6M HCl, 1 day, 100^{o}C). For three samples with high Zr contents (DR7-5, DR11-9, DR12-41), a second acid-leached powder split was dissolved at high pressure (3:1 HF–HNO_3, 2 days, 160^{o}C; 6M HCl, 1 day, 180^{o}C) to ensure dissolution of zircon-held Hf. Sr and Nd were extracted on EICHROM Sr-, TRU- and LN-resin (Pin et al., 2014) and Hf was extracted on EICHROM LN-resin (Münker et al., 2001). Pb was extracted on 0.1 ml columns of AG1-X8 (100–200 mesh) anion exchange resin (Kamber & Gladu, 2009).

All isotopic analyses were done on a NU Plasma multi-collector ICP-MS coupled to an ARIDUS desolvating device, with typical signals of 6–8V Sr, 10–20V Nd–Hf and 8–12V Pb (Maas et al., 2015; Yaxley et al., 2013). Instrumental mass bias for Sr, Nd and Hf corrected by internal normalisation to $^{88}Sr/^{86}Sr = 8.37521$, $^{146}Nd/^{144}Nd = 0.7219$ and $^{179}Hf/^{177}Hf = 0.7325$, respectively, using the exponential law. $^{87}Sr/^{86}Sr$, $^{143}Nd/^{144}Nd$ and $^{176}Hf/^{177}Hf$ ratios in unknowns are reported relative to SRM987 = 0.710230, La Jolla = 0.511860 and JMC475 = 0.282160. Internal precision (2se) is ± 0.000020 (Sr), ≤± 0.000014 (Nd), ± 0.000008 (Hf); external precision (2sd) is ± 0.000040 (Sr); ± 0.000020 (Nd), ± 0.000015 (Hf). ε_{Nd} and ε_{Hf} values were calculated for a modern Bulk Earth composition of $^{147}Sm/^{144}Nd = 0.1960$, $^{143}Nd/^{144}Nd = 0.512632$, $^{176}Lu/^{177}Hf = 0.0336$ and $^{176}Hf/^{177}Hf = 0.282785$ (Bouvier et al., 2008). Mass bias in Pb isotope runs corrected using the thallium doping technique of Woodhead (2002); for total Pb signals near 10V, this produces external precisions of ± 0.04–0.09% (2sd). Results (± 2sd external) for various isotopic and rock standards over the period 2009–2010: modern seawater, EN-1 0.709163 ± 31 (n = 25), E&A 0.708010 ± 42 (n = 7), BCR-2 0.705004 ± 39 (n = 10), 0.512644 ± 24 (n = 11), 0.282878 ± 13 (n = 9), BHVO-2 0.703456 ± 37 (n = 4), 0.512985 ± 16 (n = 7), 0.83113 ± 17 (n = 9), JNd-1 0.512115 ± 11 (n = 12). Pb isotope results for unleached BCR-2 over the period 2010–2011 (n = 22): 18.759 ± 0.039%, 15.621± 0.064%, 38.730 ± 0.087%. All results are consistent with TIMS reference values.

Age corrections were calculated with parent/daughter ratios based on ICP-MS trace element data for separate splits of the same sample powders (see Table 4). The precision of the resultant parent/daughter ratios is conservatively assumed to be ± 5%. Age corrections for Nd and Hf isotopes are very small, with negligible additional uncertainty beyond external precisions on measured $^{143}Nd/^{144}Nd$ and $^{176}Hf/^{177}Hf$, equivalent to ± 0.5 ε_{Nd} and ± 0.6 ε_{Hf} units (± 2sd).

Uncertainties in age-corrected $^{87}Sr/^{86}Sr$ have been simulated by Monte Carlo modelling and range from ± 0.00004 to 0.00012 (2sd) for the Rb/Sr range observed in the basalts ($^{87}Rb/^{86}Sr$ 0.03–1.13, ± 5%, age ± 2Ma). Rhyolite DR12-41 with $^{87}Rb/^{86}Sr = 3.65$ has a propagated uncertainty of ± 0.00039 in initial $^{87}Sr/^{86}Sr$, ca. 10x the external precision of measured $^{87}Sr/^{86}Sr$. Propagated absolute uncertainties in initial $^{206}Pb/^{204}Pb$, $^{207}Pb/^{204}Pb$ and $^{208}Pb/^{204}Pb$ isotope ratios are ± 0.01 (0.03), <± 0.01, ± 0.03 (0.04), respectively (numbers in brackets are for samples with highest U/Pb and Th/Pb, respectively). Decay constants: ^{87}Rb 1.395×10^{-11}/y; ^{147}Sm 6.54×10^{-12}/y; ^{176}Lu 1.865×10^{-11}/y; ^{238}U 0.155125×10^{-9}/y, ^{235}U 0.98485×10^{-9}/y, ^{232}Th 0.049475×10^{-9}/y.

Table A5 Whole rock radiogenic isotope compositions, with replicates after low-pressure (LP) and high-pressure (HP) dissolution.

Sample #	3-2 basalt	7-5 LP dolerite	7-5 HP dolerite	7-11 basalt	10-39 dol/gabb	11-9 LP basalt	11-9 HP basalt	12-20 dolerite	12-41 LP rhyolite	12-41 HP rhyolite	13-7 dolerite	20-1 basalt
SiO_2 wt%	54.28	53.23	53.23	51.27	49.54	55.75	55.75	54.27	75.47	75.47	49.61	55.66
MgO wt%	1.14	3.42	3.42	7.26	6.52	2.68	2.68	4.00	0.79	0.79	5.35	3.77
Rb ppm	85.6	50.2	50.2	1.99	10.34	77.3	77.3	71.9	129.2	129.2	12.12	71.1
Sr ppm	478.4	213.0	213.0	191.2	253.4	290.0	290.0	224.1	102.6	102.6	158.5	181.7
$^{87}Rb/^{86}Sr$	0.518	0.683	0.683	0.03	0.118	0.772	0.772	0.928	3.65	3.65	0.221	1.132
$^{87}Sr/^{86}Sr$	0.713171	0.714781	0.714607	0.707639	0.70383	0.712857	0.712846	0.711437	0.724667	0.724088	0.704974	0.713197
Sm ppm	12.72	10.66	10.66	3.51	4.74	11.38	11.38	5.93	14.84	14.84	1.83	5.64
Nd ppm	54.34	42.35	42.35	10.75	14.11	49.57	49.57	22.11	80.81	80.81	5.57	24.14
$^{147}Sm/^{144}Nd$	0.142	0.152	0.152	0.198	0.203	0.139	0.139	0.139	0.111	0.111	0.199	0.141
$^{143}Nd/^{144}Nd$	0.512221	0.512134	0.512121	0.512369	0.512858	0.512087	0.512094	0.512309	0.511736	0.51175	0.512816	0.512226
ε_{Nd} now	–8.0	–9.7	–10.0	–5.1	4.4	–10.6	–10.5	–6.3	–17.5	–17.2	3.6	–7.9
Lu ppm	0.67	0.92	0.92	0.36	0.34	0.69	0.69	0.49	0.97	0.97	0.24	0.67
Hf ppm	6.35	7.9	7.9	2.32	2.2	8.14	8.14	3.81	11.46	11.46	1.21	4.01
$^{176}Lu/^{177}Hf$	0.015	0.0165	0.0165	0.022	0.0219	0.012	0.012	0.0183	0.012	0.012	0.0282	0.0237
$^{177}Hf/^{177}Hf$	0.282341	0.282444	0.282462	0.282683	0.282919	0.282396	0.282402	0.282694	0.282211	0.282203	0.282974	0.282588
ε_{Hf} now	–15.7	–12.1	–11.4	–3.6	4.7	–13.8	–13.5	–3.2	–20.3	–20.6	6.7	–7.0
U ppm	0.72	0.86	0.86	0.23	0.23	0.56	0.56	0.44	2.21	2.21	0.15	0.69
Th ppm	1.78	5.4	5.4	1.15	0.61	3.93	3.93	3.04	36.92	36.92	0.22	5.95
Pb ppm	10.91	13.03	13.03	4.26	4.23	15.90	15.90	4.61	30.31	30.31	0.45	7.14
$^{238}U/^{204}Pb$	4.1	4.2	4.2	3.4	3.4	2.2	2.2	6.0	4.6	4.6	20.9	6.2
$^{232}Th/^{204}Pb$	10.6	27.1	27.1	17.6	9.4	15.9	15.9	43.2	79.9	79.9	31.7	54.9
$^{206}Pb/^{204}Pb$	17.618	17.822	17.817	17.793	18.327	17.277	17.290	17.727	17.539	17.537	17.867	17.885
$^{207}Pb/^{204}Pb$	15.671	15.684	15.68	15.637	15.602	15.592	15.588	15.622	15.632	15.631	15.597	15.664
$^{208}Pb/^{204}Pb$	38.253	38.654	38.633	38.464	38.186	38.15	38.151	38.989	39.241	39.219	38.146	39.267
$^{87}Sr/^{86}Sr_i$	0.71223	0.71354	0.71337	0.70758	0.70362	0.71146	0.71144	0.70975	0.71804	0.71746	0.70457	0.71114
$^{143}Nd/^{144}Nd_i$	0.512100	0.512005	0.511992	0.512201	0.512685	0.511969	0.511976	0.512191	0.511642	0.511656	0.512647	0.512106
ε_{Ndi}	–7.1	–9.0	–9.2	–5.2	4.3	–9.7	–9.5	–5.4	–16.1	–15.8	3.5	–7.0
$^{176}Hf/^{177}Hf_i$	0.282305	0.282404	0.282422	0.282630	0.282866	0.282367	0.282373	0.282650	0.282182	0.282174	0.282906	0.282530
ε_{Hfi}	–14.1	–10.6	–9.9	–2.6	5.8	–11.9	–11.7	–1.9	–18.4	–18.7	7.2	–6.1
$^{206}Pb/^{204}Pb_i$	17.53	17.74	17.73	17.72	18.26	17.23	17.25	17.60	17.45	17.44	17.44	17.76
$^{207}Pb/^{204}Pb_i$	15.67	15.68	15.68	15.63	15.60	15.59	15.59	15.62	15.63	15.63	15.58	15.66
$^{208}Pb/^{204}Pb_i$	38.18	38.48	38.46	38.35	38.13	38.05	38.05	38.71	38.73	38.70	37.94	38.91

References

Black, L., & Gulson, B. (1978). The age of the Mud Tank carbonatite, Strangways Range, Northern Territory. *BMR Journal of Australian Geology and Geophysics, 3*, 227–232.

Black, L., Kamo, S., Allen, C., Aleinikoff, J., Davis, D., Korsch, R., & Foudoulis, C. (2003). TEMORA 1: a new zircon standard for Phanerozoic U–Pb geochronology. *Chemical Geology, 200*, 155–170.

Bouvier, A., Vervoort, J., & Patchett, J.P. (2008). The Lu–Hf and Sm–Nd isotopic composition of CHUR: Constraints from unequilibrated chondrites and implications for the bulk composition of terrestrial planets. *Earth and Planetary Science Letters, 272*, 48–57.

Deino, A., & Potts, R. (1990). Single-crystal $^{40}Ar/^{39}Ar$ dating of the Olorgesailie Formation, Southern Kenya Rift. *Journal of Geophysical Research, 96*, 8453–8470.

Falloon, T. J., Danyushevsky, L. V., Crawford, T. J., Maas, R., Woodhead, J. D., Eggins, S. M., Bloomer, S. H., Wright, D. J., Zlobin, S. K., & Stacey, A.R. (2007). Multiple mantle plume components involved in the petrogenesis of subduction-related lavas from the northern termination of the Tonga Arc and northern Lau Basin: Evidence from the geochemistry of arc and backarc submarine volcanics, *Geochemistry, Geophysics, Geosystems, 8,* Q09003, doi:10.1029/2007GC001619

Fleck, R. J., Sutter, J. F., & Elliot, D. H. (1977). Interpretation of discordant $^{40}Ar/^{39}Ar$ age-spectra of Mesozoic tholeiites from Antarctica. *Geochimica et Cosmochimica Acta, 41*, 15–32.

Harris, A., Allen, C., Bryan, S., Campbell, I., Holcombe, R., & Palin, J. (2004). ELA-ICP-MS UPb zircon geochronology of regional volcanism hosting the Bajo de la Alumbrera Cu–Au deposit: implications for porphyry-related mineralization. *Mineralium Deposita, 39*, 46–67.

Kamber, B. S., & Gladu, A. H. (2009). Comparison of Pb purification by anion-exchange resins methods and assessment of long-term reproducibility of Th/U/Pb ratio measurements by quadrupole ICP-MS. *Geostandards and Geoanalytical Research, 33*, 169–181.

Lee, J.-Y., Marti, K., Severinghaus, J. P., Kawamura, K., Yoo, H.-S., Lee, J. B., & Kim, J. S. (2006). A redetermination of the isotopic abundances of atmospheric Ar. *Geochimica et Cosmochimica Acta, 70*, 4507–4512.

Ludwig K. R. (2009). Isoplot 3.75: A geochronological toolkit for Microsoft Excel. Berkeley Geochronology Center Special Publication, USA.

Maas, R., Grew, E. S., & Carson, C. J. (2015). Isotopic constraints (Pb, Rb–Sr, Sm–Nd) on the sources of Early Cambrian pegmatites with boron and beryllium minerals in the Larseman Hills, Prydz Bay, Antarctica. *The Canadian Mineralogist, 53*, 249–272.

McDougall, I., & Harrison, T. M. (1999). *Geochronology and Thermochronology by the $^{40}Ar/^{39}Ar$ Method.* (2^{nd} edition). Oxford University Press, New York.

Münker, C., Weyer, S., Scherer, E., & Mezger, K. (2001). Separation of high field strength elements (Nb, Ta, Zr, Hf) and Lu from rock samples for MC-ICPMS measurements. *Geochemistry Geophysics Geosystems, 2*, doi: 10.1029/2001GC000183

Paton, C., Woodhead, J. D., Hellstrom, J. C., Hergt, J. M., Greig, A., & Maas, R. (2010). Improved laser ablation U-Pb zircon geochronology through robust downhole fractionation correction. *Geochemistry, Geophysics, Geosystems, 11*, Q0AA06, doi:10.1029/2009GC002618.

Petrus, J. A., & Kamber, B. S. (2012). VizualAge: A Novel Approach to Laser Ablation ICP-MS U-Pb Geochronology Data Reduction. *Geostandards and Geoanalytical Research, 36*, 247–270.

Pin, C., Gannoun, A., & Dupont, A. (2014). Rapid, simultaneous separation of Sr, Pb and Nd by extraction chromatography prior to isotope ratios determination by TIMS and MC-ICP-MS. *Journal of Analytical Atomic Spectrometry, 29*, 1858–1870.

Renne, P. R., Balco, G., Ludwig, K. R., Mundil, R, & Min, K. (2011). Response to the comment by W.H. Schwaz et al. on "Joint determination of the ^{40}K decay constants and $^{40}Ar^*/^{40}K$ for the Fish Canyon sanidine standard, and improved accuracy for $^{40}Ar/^{39}Ar$ geochronology" by Paul R. Renne et al. (2010), *Geochimica et Cosmochimica Acta, 75*, 5097–5100.

Renne, P. R., Cassata, W. S., & Morgan, L. E. (2009). The isotopic composition of atmospheric argon and $^{40}Ar/^{39}Ar$ geochronology: Time for a change? *Quaternary Geochronology, 4*, 299–298.

Sack, P. J., Berry, R. F., Meffre, S., Falloon, T. J., Gemmell, J. B., & Friedman, R. M. (2011). In situ location and U–Pb dating of small zircon grains in igneous rocks using laser ablation–inductively coupled plasma–quadrupole mass spectrometry. *Geochemistry, Geophysics, Geosystems, 12*., Q0AA14, doi:10.1029/2010GC003405

Stacey J. S., & Kramers J. D. (1975). Approximation of terrestrial lead isotope evolution by a two-stage model. *Earth and Planetary Science Letters, 26*, 207–221.

Steiger, R. H., & Jäger, E. (1977). Subcommission on geochronology: Convention on the use of decay constants in geo- and cosmochemistry. *Earth and Planetary Science Letters, 36*, 359–362.

Vasconcelos, P. M., Onoe, A. T., Kawashita, K., Soares, A. J., & Teixeira, W. (2002). $^{40}Ar/^{39}Ar$ geochronology at the Instituto de Geociências, USP: instrumentation, analytical procedures, and calibration. *Annals of the Brazilian Academy of Sciences, 74*, 297–342.

Woodhead, J. (2002). A simple method for obtaining highly accurate Pb isotope data by MC-ICP-MS. *Journal of Analytical Atomic Spectrometry, 17*, 1381–1385.

Yaxley, G. M., Kamenetsky, V. S., Nichols, G. T., Maas, R., Belousova, E., Rosenthal, A., & Norman, M. (2013). The discovery of kimberlites in Antarctica extends vast Gondwanan Cretaceous province. *Nature Communications, 4*, 2921 doi: 10.1038/ncomms3921

York, D. (1969). Least squares fitting of a straight line with correlated errors. *Earth and Planetary Science Letters, 5*, 320–324.

Yu, Z., Robinson, P., & McGoldrick, P. J. (2001). An evaluation of methods for the chemical decomposition of geological materials for trace element analysis using ICP-MS. *Geostandards Newsletters, 25*, 199–217.

Yu, Z., Robinson, P., Townsend, A. T., Münker, C., & Crawford, A. J. (2000). Determination of high field strength elements, Rb, Sr, Mo, Sb, Cs, Tl and Bi at ng/g levels in geological reference materials by magnetic sector ICP-MS after HF/HClO4 high pressure digestion. *Geostandards Newsletter 24*, 39–50.